Unveiling the mechanism of enhanced water purification by F-Fe-Zn-MCM-41 in O_3/PMS

Weirui Chen [a], Yingjing Tian [a], Dongpo Liu [b], Yunqiang Yi [c], Xukai Li [b], Jing Wang [b], Liying Bin [a], Ping Li [a], Bing Tang [a], Laisheng Li [b,*]

[a] Guangdong Key Laboratory of Environmental Catalysis and Health Risk Control, School of Environmental Science and Engineering, Institute of Environmental Health and Pollution Control, Guangdong University of Technology, Guangzhou 510006, China
[b] School of Environment, South China Normal University, Key Laboratory of Theoretical Chemistry of Environment Ministry of Education, Guangdong Provincial Engineering Technology Research Center for Drinking Water Safety, Guangdong Provincial Key Lab of Functional Materials for Environmental Protection, Guangzhou 510006, China
[c] College of Resources and Environment, Zhongkai University of Agriculture and Engineering, Guangzhou 510006, China

ARTICLE INFO

ABSTRACT

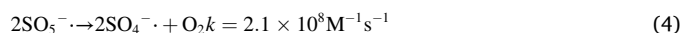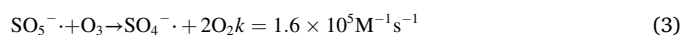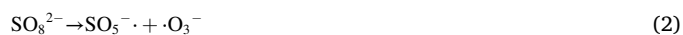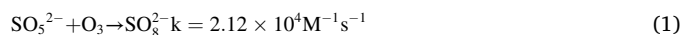To break the restriction of SO_5^{2-} as the essential initiator in O_3/PMS reaction during water purification, F-Fe-Zn-MCM-41 (FFeZn-M) was designed to enhance ibuprofen (IBP) degradation during O_3/PMS process. The great electronegativity difference between Fe and Zn created an electron flow from Zn to Fe, which was further enhanced by electron withdrawing Si-F group. FFeZn-M changed the traditional interaction between PMS and O_3. PMS would be adsorbed on the surface of Zn and acted as an electron donor. Meanwhile, O_3 received electrons from Fe site and was activated into ROS. With •OH and $^1O_2$ as the main ROS, FFeZn-M/O_3/PMS process achieved the complete IBP removal and a 60.9% mineralization rate, which was significantly higher over those of FFeZn-M/O_3 and FFeZn-M/PMS processes. FFeZn-M/O_3/PMS behaved better at weak acidic and neutral condition rather than the basic condition required by conventional O_3/PMS process. This study offered a novel catalyst design strategy for O_3/PMS.

1. Introduction

With the development of industrialization, the types and amounts of contaminants like new pollutants in natural water continued to increase, posing a serious threaten to water quality and safety [1,2]. Therefore, researchers were committed to the development of effective water treatment technologies. Recently, there was a growing interest in the synergistic effect of O_3 and peroxymonosulfate (PMS) on the degradation of organic pollutants. Coupling O_3 with PMS not only improved O_3 and PMS utilization rate but also generated several strong oxidizing free radicals like sulfate radical (SO_4•⁻) and hydroxyl radical (•OH), which oxidized pollutants more thoroughly [3,4].

As shown in Eq.1~7, there were several steps for generating SO_4•⁻ and •OH during O_3/PMS process [5]. Compared with other reactions, the reaction rate between SO_5^{2-} and O_3 (Eq.1) was much lower, which was considered as the rate-limiting step for producing SO_4•⁻ and •OH. Additionally, HSO_5^- had a dissociation constant of 9.4. When pH< 9.4, PMS mainly existed in the form of HSO_5^-, which seriously hindered O_3

activation [6]. A basic pH condition was required to obtain the satisfied treatment efficiency. But such requirement was unrealistic in practical application. On one hand, during pollutants degradation process, small molecule carboxylic acids would generate and lead to the inevitably pH decrease [7]. On the other hand, the increase of OH^- would transform SO_4•⁻ into •OH. Compared with SO_4•⁻, •OH had the weaker oxidation ability and shorter lifetime [8].
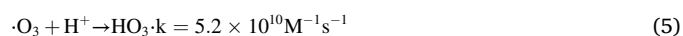
$$SO_5^{2-} + O_3 \rightarrow SO_8^{2-} \quad k = 2.12 \times 10^4 M^{-1}s^{-1} \tag{1}$$

$$SO_8^{2-} \rightarrow SO_5^- \cdot + \cdot O_3^- \tag{2}$$

$$SO_5^- \cdot + O_3 \rightarrow SO_4^- \cdot + 2O_2 \quad k = 1.6 \times 10^5 M^{-1}s^{-1} \tag{3}$$

$$2SO_5^- \cdot \rightarrow 2SO_4^- \cdot + O_2 \quad k = 2.1 \times 10^8 M^{-1}s^{-1} \tag{4}$$

$$\cdot O_3^- + H^+ \rightarrow HO_3 \cdot \quad k = 5.2 \times 10^{10} M^{-1}s^{-1} \tag{5}$$

$$HO_3 \cdot \rightarrow O_2 + \cdot OH^- \quad k = 1.1 \times 10^5 M^{-1} s^{-1} \tag{6}$$

$$SO_4^- \cdot + OH^- \rightarrow SO_4^{2-} + \cdot OH \quad k = 6.5 \times 10^7 M^{-1} s^{-1} \tag{7}$$
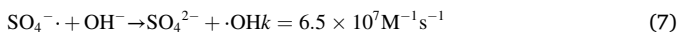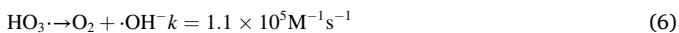
To address these issues, heterogeneous O_3/PMS system was designed. For instance, Liao et al. used Co/CMK-3 to activate O_3/PMS process for the removal of acetaminophen (AP). They found that Co/CMK-3/O_3/PMS had a higher reaction kinetic constant for degrading AP than that of O_3/PMS [6]. Jaafarzadeh et al. found that 2,4-dichlorophenoxy removal by $CuFe_2O_4$/O_3/PMS process reached 100% with $^1O_2$ serving as the major contributing species [9]. Nguyen et al. designed the Co_2SnO_4@rGO catalyst and found that there was a great synergistic effect between O_3 and Co_2SnO_4 @rGO/PMS, which triggered the non-radical and the radical mechanism for cefalexin oxidation [10].

The affinities of O_3 and PMS toward catalysts as well as their subsequent electron behavior with catalysts were vital for the efficiency of heterogeneous O_3/PMS process [11]. Our previous study suggested that F-Fe-MCM-41 had high affinity toward O_3 [12,13]. Because of their similar peroxy configuration, O_3 and PMS would compete for the Fe active site (known as Lewis acid site), which did not benefit their synergistic function [11,14]. Bimetallic silicon-based molecular sieve had strong redox ability and electron transfer performance, therefore, it was recognized as a good candidate in heterogeneous catalytic systems [15–17]. Several studies had reported that Zn could regulate the electron dispersion around active metals and boost mass transfer of PMS, which facilitated PMS activation. For instance, Chen et al. found that the existence of Zn-N sites on ZIF-67 @ZIF-8 derived carbonaceous catalyst could enhance PMS adsorption and $^1O_2$ generation [18]. The lower electronegativity of Zn in comparison to Fe would establish a local potential difference, thereby promoting the electron migration across interfaces [19]. PMS adsorption would predominantly occur at Zn site and act as electron donor [18]. The Fe-O-Zn unit could directionally convey electron to Fe for activating O_3. Therefore, the activation of O_3 and PMS on Fe-Zn co-doping MCM-41 was thermodynamically feasible. Additionally, the simultaneous presence of F element further polarized the surface electrons because of its strong electron withdrawing ability, thereby promoting electron transfer and facilitating the reactive oxygen species (ROS) production [20,21].

In this study, F-Fe-Zn-MCM-41 (FFeZn-M) was utilized in O_3/PMS process with the interfacial potential difference zone (Fe and Zn centers) acting as active sites. IBP was a common used pharmaceutical and personal care products (PPCPs). It had great potential ecological hazards [22]. Various kinds of technologies were developed to treat with IBP, including ozonation, photocatalysis, non-thermal plasma and PS based processes [23,24]. Results showed that IBP was stable to sole ozonation and PS process, with the low mineralization rate were obtained. Though photocatalytic ozonation and DBD plasma could achieve the high degree of mineralization, they were energy consuming. Therefore, IBP was selected as model pollutant to explore the activity of FFeZn-M in O_3/PMS process. The interfacial electron transfer mechanisms were revealed by various techniques including in situ Raman, ATR-FTIR, XPS, electrochemical testing and DFT calculations. In addition, EPR and scavenger experiments were conducted to identify the involved active species. These findings provided insight into the underlying mechanism of heterogeneous O_3/PMS process induced by FFeZn-M.

2. Experimental details

2.1. Catalyst synthesis

All the used reagents could be found in Text S1. As shown in scheme S1(a), the hydrothermal method was adopted to prepare FFeZn-M with $FeF_3 \bullet 3 H_2O$ serving as the iron and fluorine source and $ZnSO_4 \bullet 7 H_2O$ serving as the zinc source, respectively [25]. 0.1 M $Na_2SiO_3 \bullet 9 H_2O$ was dissolved with metal source in 75 mL deionized water with the Si/metal ratio of 120. H_2SO_4 was used to assist the transformation of solution into

gel, which was then followed the dissolve of 7.28 g CTAB. The mixed solution underwent crystallization at 145 ℃ for 2 d. The resulting material was dried and then calcined in a muffle furnace at 550 ℃ for 6 h to get FFeZn-M. Morphology characterization, physical and chemical properties of prepared catalysts were enclosed in Text S2.

2.2. Experimental protocols

As shown in scheme S1(b), IBP degradation was carried out in a double-layer glass reactor (inner diameter/outer diameter/height of 80/100/300 mm). The ozone generator (ANSEROS) was used to produce O_3 and O_3 came into reactor via the sand core gas distribution plate at the bottom of reactor. The temperature was controlled by circulating cooling water. The reaction condition was under the following parameters unless special statement: IBP concentration: 10 mg L^{-1}; initial pH: 5.0; total volume: 1.0 L; PS dosage: 0.4 g/L; O_3 output: 50 mg/h; flow rate: 1.0 L/min, catalyst concentration: 0.5 g/L.

2.3. Analysis methods

All water samples were filtered with a 0.45 μm filter before analysis. The concentration of IBP was determined using a high-performance liquid chromatograph with UV detector (SPD-16) and a WondaSil C18-WR column (150 mm × 4.6 mm). The mobile phase was prepared by combining aqueous buffer solution (50 mL of methanol, 1 mL of ultrapure water, and 4 mL of phosphoric acid) and acetonitrile in a 4:6 vol ratio. The detection wavelength was set as 230 nm, the injection volume was set as 100 μL, and the flow rate was set as 1.0 mL min^{-1}. The total organic carbon content of the sample was determined using a TOC analyzer, while the ozone concentration at the inlet and outlet was measured using a portable ozone detector. The intermediate products of IBP degradation were determined using gas chromatography-mass spectrometry (GC-MS, Shimadzu). The product was dissolved in dichloromethane with an injection volume of 1.0 μL. Chromatographic conditions: The initial column temperature is maintained at 40 °C for 3 min, followed by a heating rate of 10 °C min^{-1} to 200 °C. The ABTS method was used to measure the concentration of PMS [26]. The indigo method is used to measure the concentration of ozone in solution [27]. The zero charge point of the catalyst was determined using a Malvern Zetasizer Nano ZS90 nanoparticle potential meter. Gaussian 16 was adopted to carried out the DFT calculation [28]. More details information on DFT calculation could be found in Text S3.

3. Results and discussion

3.1. Characterizations

Textural properties of FFeZn-M were explored by XRD, TEM and N_2 adsorption-desorption curves. XRD patterns of all catalysts exhibited comparable signals at ~2.2, ~3.8, and ~4.4°, corresponding to their (100), (110), and (200) planes (Fig. S1) [19]. Compared with those of MCM-41, FeZn-M exhibited the diffraction peaks at the smaller angles. The observed phenomenon could be attributed to the larger atomic radii of Fe^{3+} and Zn^{2+} compared to Si^{4+} (0.63 Å vs. 0.60 Å vs. 0.40 Å) [29]. The introduction of Si-F group caused a left shift of the (100) plane of FFeZn-M compared to that of FeZn-M [12]. By comparing the TEM images of Fe-M, FeZn-M and FFeZn-M (Fig. S2(a-f)), it was evident that FFeZn-M (Fig. S2(e-f)) exhibited a highly ordered mesoporous structure with unobstructed pores, which could be attributed the elimination of the incompletely hydrolyzed condensed silicon and metal oxides by HF [13]. F, Fe, and Zn were homogeneous distributed with Si and O, and their atomic percentage accounted for 0.8%, 0.3%, and 0.27% (Fig. S2 (g-l)). The actual content of Fe and Zn in FeZn-M and FFeZn-M were measured by ICP and their contents were almost identical (Fe: 0.022 vs 0.021 mg g^{-1}; Zn: 0.022 vs 0.025 mg g^{-1}). The actual F content was measured as 0.073 mg g^{-1}. N_2 adsorption desorption curves of MCM-41,

FeZn-M and FFeZn-M were all belonged to typical IV (Fig. S3), implying that mesoporous structure was remained after modification. As depicted in Table S1, S_{BET} of MCM-41 was 1171.6 m^2 g^{-1}. And it was 831.6 and 721.8 m^2 g^{-1} for FeZn-M and FFeZn-M, respectively. FFeZn-M had the smaller S_{BET} but higher catalytic activity than that of FeZn-M, which further suggested potential function of Si-F group. As a three phase system, O$_3$ tended to be absorbed on hydrophobic surface during the heterogeneous O$_3$/PMS process. Therefore, thermogravimetric analysis (TG) was employed to explore the interfacial hydrophobicity. As demonstrated in Fig. 1(a), pure MCM-41 had a mass loss of 12.1%, which was higher than those of FeZn-M (8.1%) and FFeZn-M (4.3%). It seemed that metal doping could promote the condensation of silicon during hydrothermal process, and the implanting of F further replaced the silanol, which increased the surface hydrophobicity. Furthermore, as depicted in Fig. 1(b), MCM-41 and FeZn-M had a water contact angle of ~4.5° and ~38.6°. But the water contact angle of FFeZn-M was ~52.3°, which was related with the formation of hydrophobic Si-F sites. Meanwhile, MCM-41 and FeZn-M had a surface hydroxyl density of 2.12 and 1.68 mmol g^{-1}. It decreased to 1.46 mmol g^{-1} for FFeZn-M, which was consistent with results of water contact angle. The less surface hydroxyl density suggested the greater hydrophobicity. Therefore, the above results clearly demonstrated that the simultaneous incorporation of F, Fe, and Zn created both Lewis acid sites and hydrophobic sties on MCM-41.

To evaluate the influence of Zn and Si-F group on the redox property of FFeZn-M, H$_2$-TPR was employed. Fig. 2(a) showed that Fe-M had two peaks at 313 and 455 °C (indexed as α and β). The α peak was corresponded to the single electron reduction process of Fe^{3+} (Fe^{3+}→Fe^{2+}), while the β peak suggested the two electron reduction of Fe^{2+} (Fe^{2+}→Fe^0) [30]. Zn-M exhibited a reductive peak at 541 °C (indexed as γ), which was attributed to the two electron reduction of Zn^{2+} (Zn^{2+}→Zn^0) [31]. As for FeZn-M, its α peak shifted to a lower temperature at 296 °C, but the β and γ peaks shifted to the greater temperature at 493 and 543 °C, respectively. The above results suggested that doping Zn was favorable for the single reduction of Fe^{3+} to Fe^{2+} [32]. α peak of FFeZn-M further shifted toward a lower temperature (246 °C). The reductive peaks of Fe^{2+} to Fe^0 and Zn^{2+} to Zn^0 shifted to 485 and 560 °C. The above results suggested that Si-F group would enhance the internal electron migration because of its strong electron withdrawing ability, enabling the reduction of Fe^{3+} to Fe^{2+}. Meanwhile, Zn became more positively charged in FFeZn-M, indicating the inhibition of its two electron reduction process [33].

O$_2$-TPD was utilized to investigate the surface oxygen fluidity of catalysts. As depicted in Fig. 2(b), two O$_2$ desorption peaks were observed for all catalysts. The peak at ~110 °C was attributed to the chemically absorbed oxygen at oxygen vacancy while the peak at ~250–350 °C was the surface absorbed oxygen. Compared with those of Fe-M, Zn-M and FeZn-M, both O$_2$ desorption signals of FFeZn-M occurred at the lower temperature, which suggested the relatively loose oxygen bonding with metal centers and the higher oxygen fluidity. Moreover, it should be noted that the O$_2$ desorption amount of FFeZn-M was much larger over those of other catalysts, demonstrating that the great synergy of Fe and Zn could boost the mobile phase of oxygen within MCM-41′s framework and F doping facilitated for oxygen detach [14]. Combing the former results, it was reasonable to infer the easily reduction of Fe^{3+} to Fe^{2+} on FFeZn-M.

3.2. Catalytic performance of FFeZn-M in O$_3$/PMS

IBP degradations by different processes were carried out to explore the feasibility of FFeZn-M/O$_3$/PMS system. As illustrated in Fig. 3(a), sole O$_3$ led to a 30.1% IBP removal in 30 min and 9.4% TOC removal in 60 min. In the O$_3$/PMS process, IBP removal reached 67.7% and TOC removal reached 21.4%. As depicted in Eqs.(1–7), the couple of O$_3$ and PMS would trigger the generation of •OH and SO$_4$•, which enhanced the performance of sole O$_3$ [6]. Because the initial solution pH was 5.0, the activation efficiency of O$_3$ and PMS was not high, the enhancement in IBP removal and TOC removal were limited. The addition of Fe-M, Zn-M, FeZn-M and FFeZn-M further improved IBP removal in O$_3$/PMS process and their respective removal rates reached 76.8%, 81.1%, 82.6%, and 100%, respectively. The great catalytic activity of FFeZn-M could be better demonstrated by the mineralization process. After 60 min's reaction, TOC removals in Fe-M/O$_3$/PMS, Zn-M/O$_3$/PMS, FeZn-M/O$_3$/PMS, and FFeZn-M/O$_3$/PMS were 30.1%, 32.3% and 51.3%, respectively. FFeZn-M/O$_3$/PMS demonstrated the highest IBP mineralization of 60.9% (Fig. 3(b)). To further demonstrate the contribution of O$_3$ and PMS as well as the function of Fe and Zn sites, the sole O$_3$ involved and PMS involved processes were carried out. As depicted in Fig. 3(b) and Fig. 3(e), the O$_3$ involved processes exhibited the greater performance over those of PMS involved processes. For instance, FFeZn-M/O$_3$ had the IBP removal of 93.4% and TOC removal of 46.5%, but only 46.4% IBP removal and 24.8% TOC removal were obtained by FFeZn-M/PMS process. This suggested that O$_3$ contributed the more to the heterogeneous O$_3$/PMS process, which was ascribed to the continuous O$_3$ aeration. The activity of catalysts in activating O$_3$ and PMS exhibited the trend of FFeZn-M> FeZn-M>Zn-M>Fe-M. Generally, the metal centers on Fe-M and Zn-M could act as Lewis active sites for
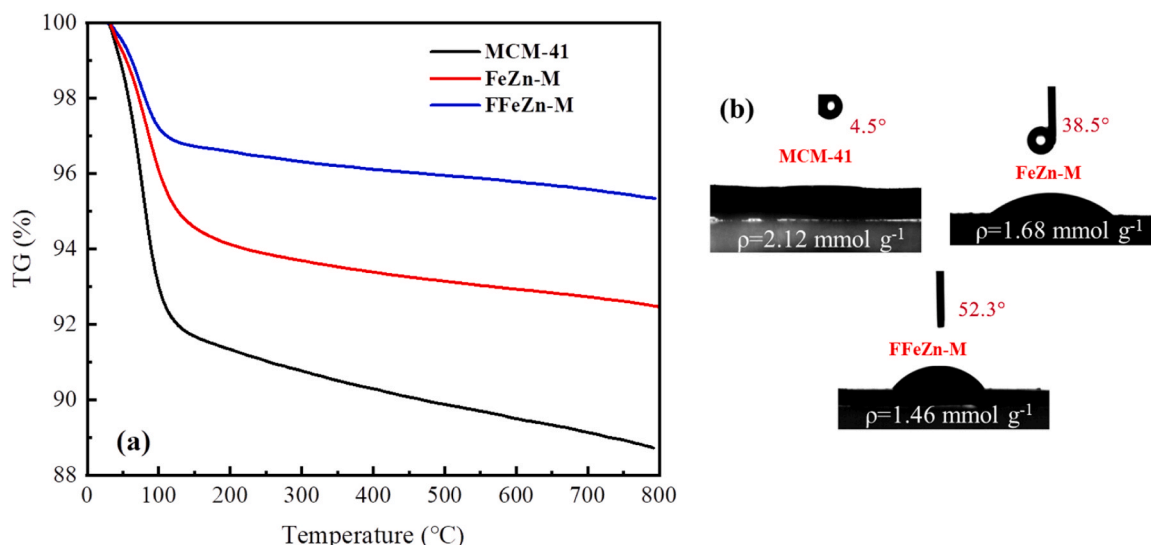

Fig. 1. (a) TG curves and (b) water contact angle and hydroxyl density of catalysts.
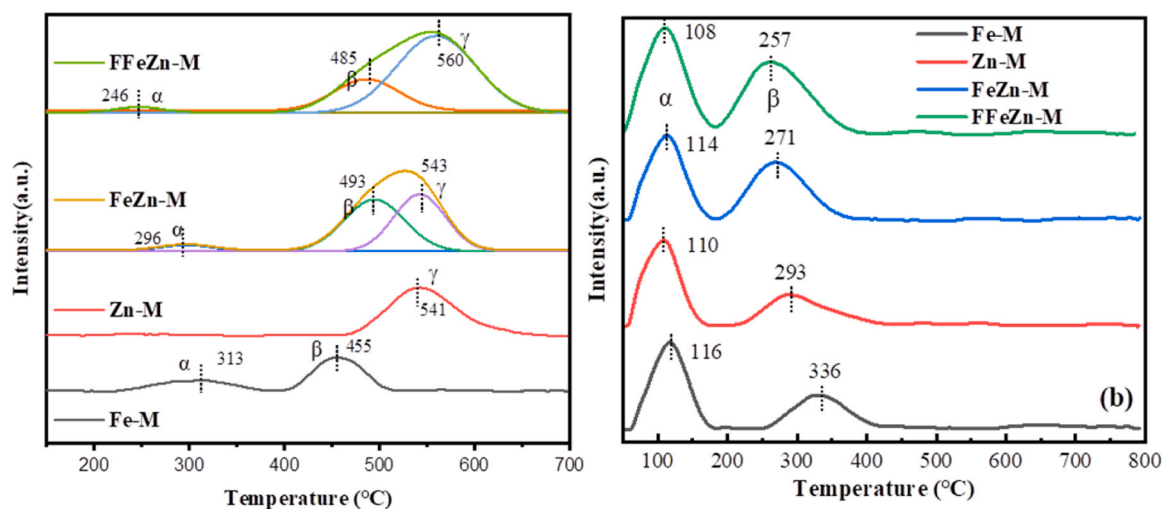
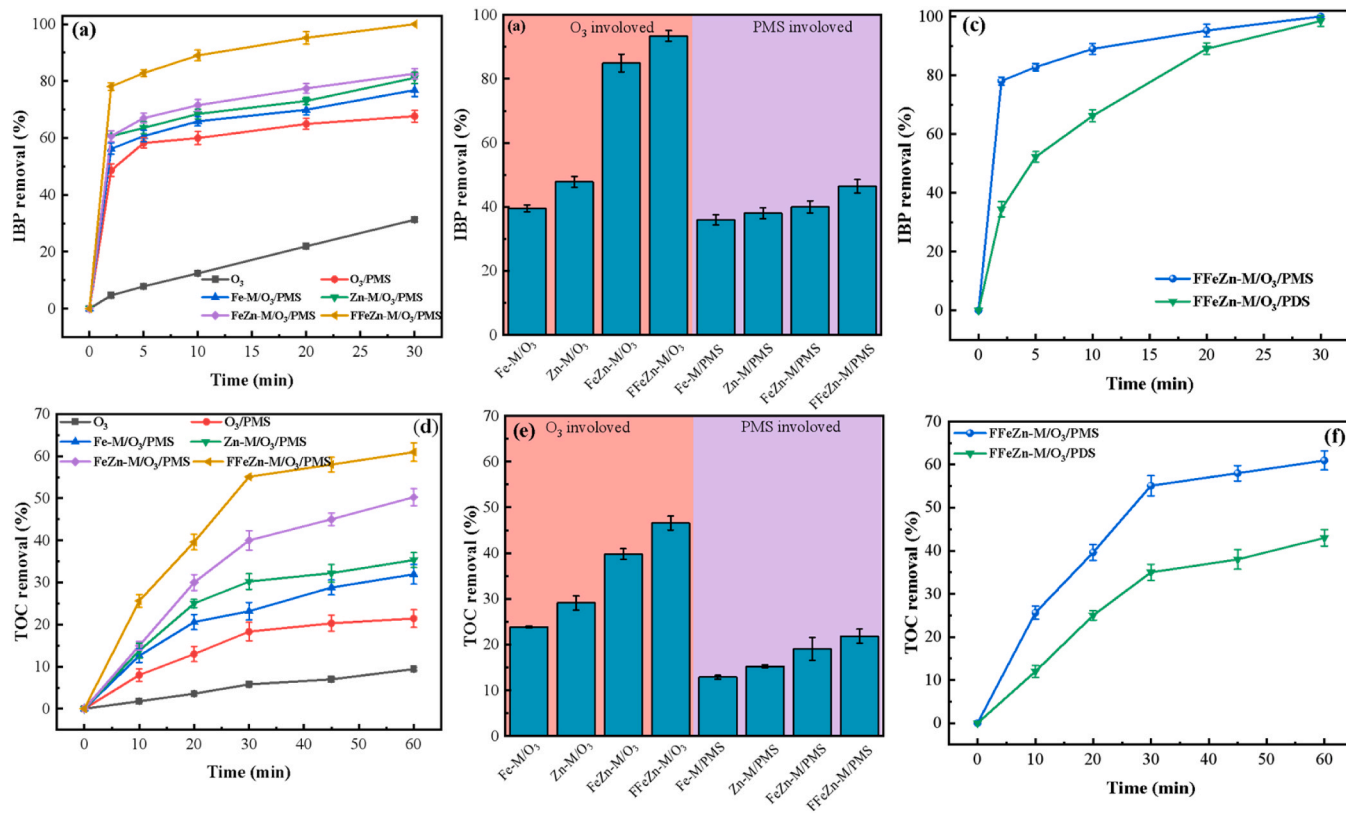**Fig. 2.** (a) H_2-TPR and (b) O_2-TPD of different catalysts.

Fig. 3. Effect of different systems on (a) IBP removal and (d) mineralization; comparative sole O_3 and PMS involved process for (b) IBP removal and (e) mineralization; Effect of different PS on the IBP removal (c) and mineralization (f) (Reaction condition: IBP concentration: 10 mg L^{-1}; initial pH: 5.0; total volume: 1.0 L; PS dosage: 0.4 g/L; O_3 output: 50 mg/h; flow rate: 1.0 L/min, catalyst concentration: 0.5 g/L).

activating O_3 and PMS [11,14]. Zn in silicon skeleton exhibited the greater Lewis acid strength over Fe, therefore, Zn-M had the greater activation efficiency over Fe-M [19]. As proposed in previous study, the co-existence of Fe and Zn in MCM-41 would establish a local potential difference because of the electronegativity discrepancy between Zn and Fe, thereby promoting the electron migration and O_3 and PMS activation efficiency [25]. With the implantation of Si-F groups, F atom with great electron attraction ability would further polar the surface electron distribution and enhance the electron migration rate on FFeZn-M, which enhanced the activation of O_3 and PMS. Meanwhile, the hydrophobic
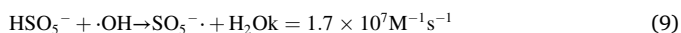
sites provided by Si-F could enhance the mass transfer of O_3 [12]. The above factors accounted for the greater activity of FFeZn-M. Moreover, it should be noted that systems with only one oxidant (O_3 or PMS) exhibited lower degradation efficiency than those where O_3 and PMS coexisted, which suggested the mutually reinforcing interaction between O_3 and PMS. When O_3 and PMS coexisted, they had difference affinity toward Zn and Fe sites on FFeZn-M (verified by DFT calculation in Section 3.4.4). The electron poor Zn sites could obtain electron from PMS and then the electron was transferred to the electron rich Fe sites for the handy activation of O_3 into $\bullet O_3^-$. Meanwhile, after donating

electron, PMS was conveyed into $SO_5\bullet$, which eventually generated $^1O_2$. Hence, the cooperation of FFeZn-M, O_3 and PMS resulted in the best performance of FFeZn-M/O_3/PMS.

PMS and PDS were commonly used in AOPs, but their couple effect with O_3 differed considerably. As illustrated in Fig. 3(c and f), after the addition of PMS or PDS, IBP removal in 2 min increased from 6.9% to 78.1% and 34.5%, respectively. Similarly, TOC removal in 60 min increased from 32.5% to 60.9% and 43.0% for FFeZn-M/O_3/PMS and FFeZn-M/O_3/PDS, respectively. Obviously, PMS had a stronger synergistic effect with FFeZn-M/O_3 over PDS. PDS had a symmetrical structure, which limited its reactivity with O_3 and reduced the reactivity of peroxy group (-O-O-) [34]. Thus, coupling FFeZn-M/O_3 with PMS could exhibit more robust synergistic effect. The feasibility of FFeZn-M/O_3/PMS process was tested with Atrazine (ATZ), Chlorbic acid (CA), Benzabate acting (BZF) as target pollutants. As shown in Fig. S4, FFeZn-M/O_3/PMS had a stronger ability to mineralize the organic pollutants compared to sole ozonation and FFeZn-M/O_3 processes. The mineralization rates of ATZ, CA, and BZF by FFeZn-M/O_3/PMS in 120 min were 67.5%, 60.6%, and 53.2%, respectively, which were higher than the mineralization rates of 16.7%, 16.4%, and 12.2% achieved by sole ozonation and the mineralization rates of 38.3%, 29.4%, and 19.1% achieved by the FFeZn-M/O_3 process.

The influence of PMS dosage on IBP removal was studied. As demonstrated in Fig. S5, both IBP and TOC removal was characterized by a gradual increase followed by a decrease with PMS dosage, with the greatest performance (93.4% IBP removal in 30 min, 60.9% TOC removal in 60 min) occurred at 0.4 g/L. There exhibited the greater amount of ROS with the increase of PMS addition. But excessive PMS would consume $\bullet$OH and $SO_4\bullet^-$ to form $SO_5\bullet$ with weaker oxidation ability, which lowered the oxidation of IBP and its intermediates (shown in Eqs.8–9) [35,36].

$$HSO_5^- + SO_4^{2-}\bullet \rightarrow SO_4^{2-} + SO_5^-\bullet + H^+ \quad k = 1.0 < 10^5 M^{-1}s^{-1} \quad (8)$$

$$HSO_5^- + \bullet OH \rightarrow SO_5^-\bullet + H_2O \quad k = 1.7 \times 10^7 M^{-1}s^{-1} \quad (9)$$
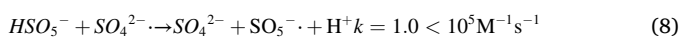
More emphasis was placed on the stability of FFeZn-M. After 60 min reaction, the leaching amounts of F, Fe, and Zn were 0.39, 0.12, and 0.36 mg L^{-1}, respectively. IBP removal and TOC removal gradually decreased in five successive uses. The IBP removal was 90.8% and TOC removal was 48.9% in the 5th run, which remained higher over that of O_3/PMS process (Fig. S6). The results suggested that FFeZn-M exhibited favorable stability and recyclability.

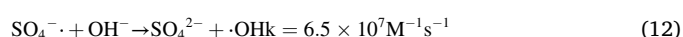### 3.3. Influence of water matrixes

3.3.1. Effects of different pH

Heterogeneous O_3/PMS process was highly sensitive to solution pH, which not only affected the chemical speciation and stability of O_3, PMS, and IBP, but also determined the electrical charge of catalyst [8,26,37]. Additionally, the change of pH would alter the transform rate of $SO_4^-\bullet$ to $\bullet$OH [8]. Therefore, the influence of initial solution pH was considered. HCl and NaOH were used to adjust the solution rather than buffer solution because the buffer salt ion pairs would shelter the surface active sites or consume the ROS [38,39]. As shown in Fig. 4(a-b), as pH raised from 3 to 5, IBP removal increased from 80.7% to 100%, and TOC removal increased from 53.4% to 60.9%. As pH further increased to 9, IBP removal gradually decreased to 78.3% and TOC removal decreased to 50.6%. Obviously, too acidic and alkaline conditions were not conducive to IBP oxidation by FFeZn-M/O_3/PMS process.

pHpzc of FFeZn-M was measured as 2.5 (Fig. S7). Therefore, during the whole tested pH, the surface of FFeZn-M was negatively charged. IBP had the pKa of 4.6, and it was positively charged at pH of 3–4.6, and turned negatively charged at pH 4.6–9. Though the electrostatics between FFeZn-M and IBP at pH= 3, IBP degradation was not high. On one hand, H$^+$ in solution would damage the structure of FFeZn-M and result in the metal leaching, which reduced the amount of active sites. On the other hand, the excessive H$^+$ would inhibit the reaction between O_3/PMS in bulk solution as well as consume the generated $\bullet$OH and $SO_4\bullet^-$ (Eqs.10–11) [26,40]. Hence, IBP degradation was poor at pH= 3. With the increase of solution pH, the reaction of homogeneous O_3/PMS became faster, but IBP removal was also not high at pH= 9, which highlighted the greater function of heterogeneous O_3/PMS reaction over the homogenous one in IBP degradation. Under alkaline conditions, $SO_4\bullet^-$ was rapidly conveyed into $\bullet$OH (Eq.12). Compared with that of
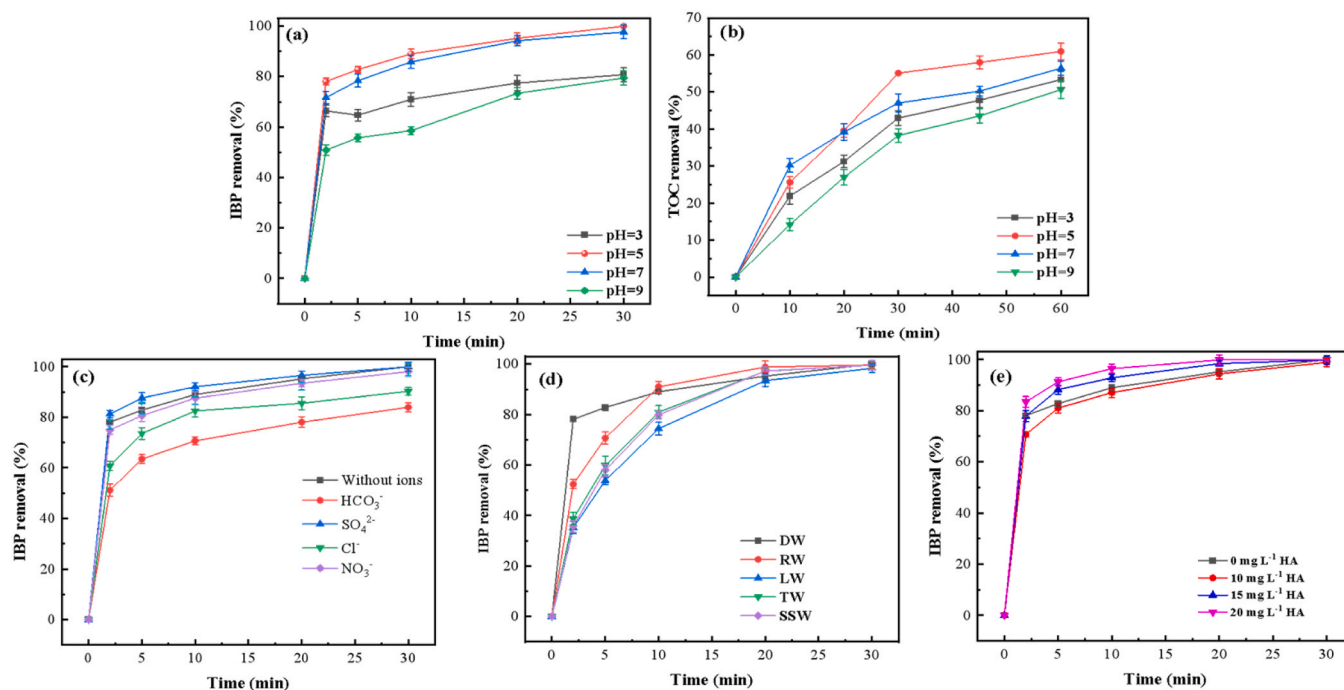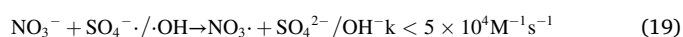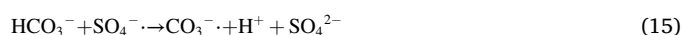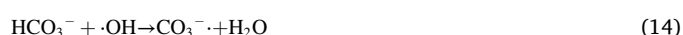

Fig. 4. Effect of different pH (a-b), coexistence ions (c), real water (d) and HA (e) on IBP degradation (Reaction condition: IBP concentration 10 mg L^{-1}; initial pH: 5.0; total volume: 1.0 L; PS dosage: 0.4 g/L; O_3 output: 50 mg/h; flow rate: 1.0 L/min, catalyst concentration: 0.5 g/L).

SO₄•⁻, •OH had the weaker oxidation ability and shorter lifetime [26,35, 41]. Furthermore, the strong electrostatic repulsion between FFeZn-M, IBP and HSO₅⁻ was also not conducive to the interfacial oxidation [10]. Thus, the performance of FFeZn-M/O₃/PMS decreased at basic condition. At pH= 5 and pH= 7, the strong electrostatic repulsion between IBP and FFeZn-M was not as strong as that of pH= 9. And PMS and O₃ could be absorbed by FFeZn-M via the hydrogen bond and electrostatic attraction function [14,26]. Under the function of surface great potential difference induced by F, Fe and Zn, the electron migration among PMS, O₃ and FFeZn-M was enhanced, generating more ROS to degrade IBP. And it should be noted that the traditional O₃/PMS process typically performed well as basic condition. But in our study, FFeZn-M/O₃/PMS process showed the better efficiency at pH= 5 and pH= 7, which suggested that the interfacial reaction of O₃ and PMS on FFeZn-M was different from that in bulk solution.

$$SO_4^- \cdot + H^+ + e^- \rightarrow HSO_4^- \cdot \tag{10}$$

$$\cdot OH + H^+ + e^- \rightarrow H_2O \tag{11}$$

$$SO_4^- \cdot + OH^- \rightarrow SO_4^{2-} + \cdot OH \quad k = 6.5 \times 10^7 M^{-1}s^{-1} \tag{12}$$

3.3.2. Influence of inorganic ion

Fig. 4(c) demonstrated that except for SO_4^{2-}, the presence of HCO_3^-, Cl⁻ and NO_3^- hindered IBP removal, with IBP removal decreased from 100% to 83.9%, 90.3%, and 98%, respectively. As shown in Eq.13, the reaction between •OH and SO_4^{2-} could generate SO₄•⁻ with stronger oxidation ability, thereby accelerating IBP degradation. Among the tested ions, HCO_3^- had the most significant inhibition. As shown in Eqs.14–15, HCO_3^- could react with both •OH and SO₄•⁻ to generate low-reactive CO₃•⁻ (E₀ =1.78 V), and it could also hinder the activation of PMS and O₃ by occupying the active site on FFeZn-M [42,43]. Similarly, Cl⁻ hindered IBP degradation by consuming •OH and SO₄•⁻ to generate Cl• (E₀ =2.6 V) as well as directly reacting with PMS and O₃ (Eqs.(16–18)) [9]. Compared with other ions, the reaction rates of NO_3^- with •OH and SO₄•⁻ were much lower (Eq.(19)), so its impact on IBP removal was minimal.

$$\cdot OH + SO_4^{2-} \rightarrow OH^- + SO_4^- \cdot \tag{13}$$

$$HCO_3^- + \cdot OH \rightarrow CO_3^- \cdot + H_2O \tag{14}$$

$$HCO_3^- + SO_4^- \cdot \rightarrow CO_3^- \cdot + H^+ + SO_4^{2-} \tag{15}$$

$$Cl^- + SO_4^- \cdot / \cdot OH \rightarrow Cl \cdot + SO_4^{2-}/OH^- \tag{16}$$

$$Cl^- + HSO_4^- \rightarrow SO_4^{2-} + HOCl \tag{17}$$

$$Cl^- + O_3 \rightarrow ClO^- + O_2 \tag{18}$$

$$NO_3^- + SO_4^- \cdot / \cdot OH \rightarrow NO_3 \cdot + SO_4^{2-}/OH^- \quad k < 5 \times 10^4 M^{-1}s^{-1} \tag{19}$$

3.3.3. Impact of actual water and humic acid

The feasibly of FFeZn-M/O₃/PMS process in practical scene was tested with river water (RW), lake water (LW), tap water (TW), and secondary effluent (SSW) acting as medium. The water quality parameters were enclosed in Table S2. IBP was completely removed in different actual water bodies, and k values further increased from 0.124 min⁻¹ to 0.189, 0.133, 0.180, and 0.180 min⁻¹, respectively (Fig. 4(d), Fig. S8). The dissolved organic matters in actual water like humic acid (HA) were composed of benzene and ester rings, which were enriched with carboxyl, hydroxyl, carbonyl, quinone, and methoxy functional groups. They could form complexes with metal centers on FFeZn-M, thereby promoting the conversion of Fe^{3+} to Fe^{2+} and accelerating the activation of O₃ and PMS to •OH and SO₄•⁻, and improving IBP degradation efficiency [44,45].

HA was further added to explore its impact on FFeZn-M/O₃/PMS. Noted that HA could not dissolve in acidic or neutral conditions. The HA stock solution was prepared by dissolving HA in 1% NaOH solution under 80 °C. The stock solution was diluted to a specific concentration and followed by the pH adjustment. As demonstrated in Fig. 4(e), introducing 10 mg L⁻¹ HA had negligible influence on IBP degradation, and the addition of greater amount of HA even enhanced its removal. Upon the addition of 15 and 20 mg L⁻¹ HA, IBP removal reached 88.2% and 91.3% after only 5 min, respectively, which were higher than that of FFeZn-M/O₃/PMS (82.7%). The rate constant (k) was calculated as 0.074, 0.111, 0.179, and 0.264 min⁻¹, respectively (Fig. S9). The above facts suggested that HA could promote the performance of FFeZn-M/O₃/PMS process, which was also reported by Duan et al [46]. HA could complex with IBP, accelerating the adsorption of IBP on the surface of FFeZn-M and shorting the mass transfer distance of ROS and IBP, which favored for IBP degradation. FTIR was carried out to monitor the complex of IBP and HA. As shown in Fig. S10, IBP showed the characteristic peaks at ~699, ~1061 and ~1321 cm⁻¹ for O-H, C-O and C=C groups, respectively. They all disappeared with the co-existence of HA. Moreover, the peak of HA at ~1384 and ~1028 cm⁻¹ shifted to the lower wavenumber with the co-existence of IBP [47]. The above results verified the complex of IBP with HA. The adsorption of IBP by FFeZn-M in the absence and presence of HA were explored. As shown in Fig. S11, the presence of HA significantly enhanced the adsorption efficiency of IBP by FFeZn-M, with an increase of three times compared to the absence of HA. The equilibrium adsorption capacity (Q_e) for IBP with the presence of HA was calculated as 2.55 mg g⁻¹, whereas it was only 0.67 mg g⁻¹ with the absence of HA. Moreover, during FFeZn-M/O₃/PMS process, the quinone functional groups in HA could yield semi-quinone radicals through self-oxidation-reduction reactions to promote PMS's activation into •OH and SO₄•⁻, which improved the degradation efficiency of organic pollutants [48,49].

3.4. Exploration of catalytic mechanism

3.4.1. Generation of ROSs and their contribution

As a couple systems of O₃ and PMS, there were various active radicals (mainly SO₄•⁻ and •OH) and non-radical (¹O₂), which participated in IBP degradation [10]. To investigate the IBP removal mechanism by FFeZn-M/O₃/PMS process, the existence of active species and their contributions to IBP removal were studied by EPR and quenching experiments.

After being scavenged by DMPO, DMPO-SO₄•⁻ adduct would exhibit sextet with coupling constant of $\alpha_N = 13.2$ G, $\alpha_H = 9.6$ G, $\alpha_H = 1.48$ G, $\alpha_H = 0.78$ G, and DMPO-•OH adduct would display quartet with coupling constant of $\alpha_N = \alpha_H = 14.9$ G [26]. Compared with those of FFeZn-M/O₃, FFeZn-M/PMS, O₃/PMS, and sole O₃ processes, DMPO-•OH signal in FFeZn-M/O₃/PMS process exhibited the highest strength, indicating that the couple of PMS with FFeZn-M/O₃ produced more •OH (Fig. 5(a)). Though DMPO-SO₄•⁻ signals were also found in FFeZn-M/O₃/PMS, FFeZn-M/PMS, and O₃/PMS processes, but it exhibited a very small signal when compared with that of DMPO-•OH adduct. Moreover, DMPO-SO₄•⁻ signal in FFeZn-M/O₃/PMS process was weaker than those of FFeZn-M/PMS and O₃/PMS processes. Generally, when PMS accepted external electron, it could be activated into SO₄•⁻ through a radical route. When PMS served as electron donor, it would be transformed into SO₅•⁻, which eventually yielded ¹O₂ rather than SO₄•⁻. Therefore, we considered that during FFeZn-M/O₃/PMS process, part of PMS acted as electron donor rather than acceptor because of the coexistence of O₃. Formation of ¹O₂ was monitored to verify the hypothesis. As shown in Fig. 5(b), ¹O₂ captured by TEMP generated TEMPO-¹O₂ adduct with a typical 1:1:1 triple peak ($\alpha_H = \alpha_N = 17.2$ G). ¹O₂ was detected in all reaction system, but the TEMPO-¹O₂ signal in FFeZn-M/O₃/PMS process was much stronger than those in FFeZn-M/O₃, FFeZn-M/PMS, O₃/PMS, and sole O₃ processes. ¹O₂ in sole O₃, FFeZn-M/O₃ and O₃/PMS was mainly originated from the reaction between •O₂ and secondary radicals like HO₂• and •OH (shown in Eqs.20–21) [10,38].
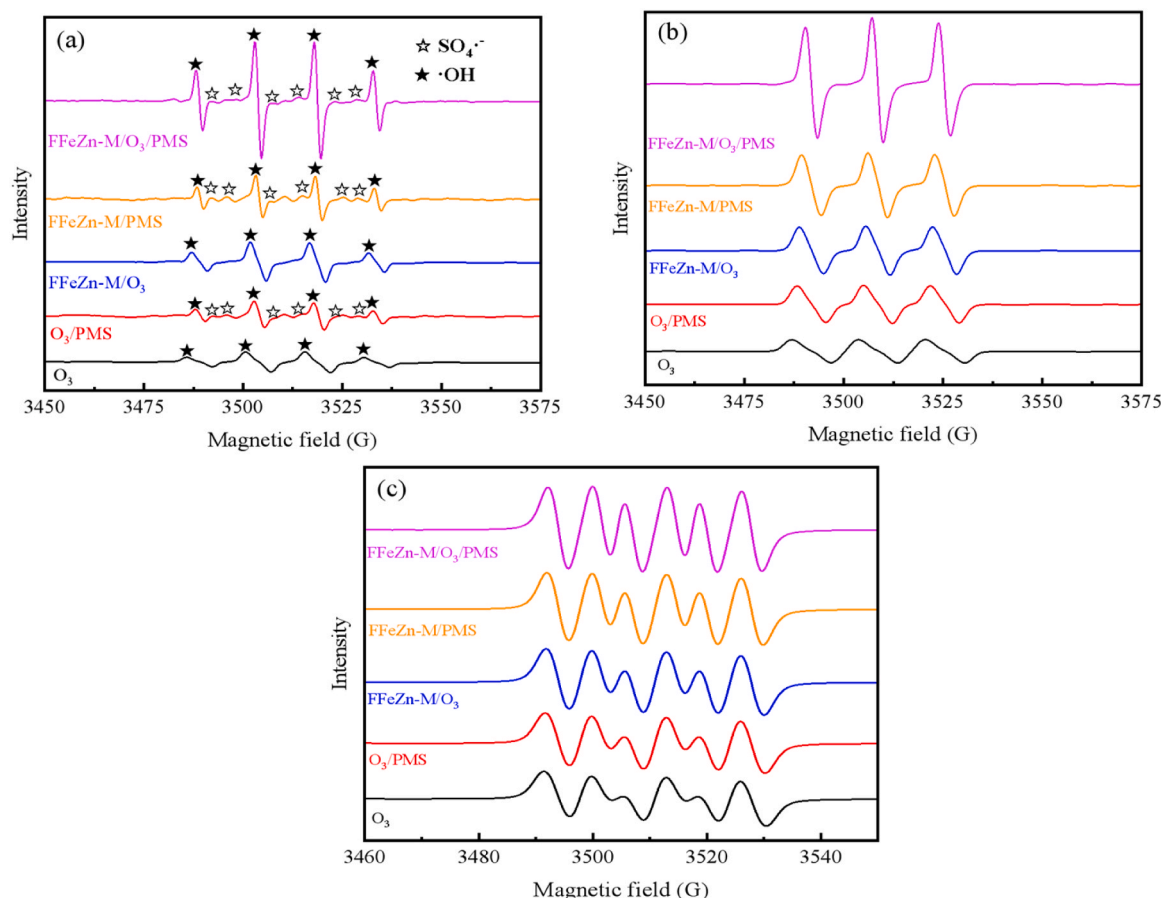
Fig. 5. Characteristic peaks of EPR spectrum for different reactive oxygen species (a) DMPO-•OH and DMPO-SO₄•; (b) TEMPO-¹O₂; (c) DMPO-•O₂.

$$O_2^- \cdot + 2HO_2 \cdot + H^+ \rightarrow {}^1O_2 + H_2O_2 \tag{20}$$

$$O_2^- \cdot + HO \cdot \rightarrow {}^1O_2 + OH^- \tag{21}$$

As shown in Fig. 5(c), DMPO-O₂•⁻ signal (with α_N =12.45 G and α_H=14.25 G) was detected for all the test systems, but unlike DMPO-•OH and TEMPO-¹O₂, no obvious difference in O₂•⁻ concentration was found [50]. The comparable levels of •O₂⁻ concentration among these processes resulted in their negligible differences in ¹O₂ production. Regarding the FFeZn-M/PMS process, the formation of ¹O₂ suggested the simultaneous occurrence of oxidative and reductive activation of PMS. As proposed by Zhu, PMS could be conveyed into ¹O₂ at electron depleted zone and •SO₄⁻ and •OH at electron rich ozone [51]. Because Fe had the greater electronegative than Zn, electron on Zn would be dragged around Zn. Therefore, in FFeZn-M/PMS process, ¹O₂ might form at Zn sites and •SO₄⁻ and •OH were might form at Fe site. When O₃ and PMS coexisted on the surface of FFeZn-M, the greatest ¹O₂ was found, demonstrating that more PMS was activated via the non-radical route because the difference in •O₂⁻ concentration was relatively minor compared to other systems (Fig. 5(c)). Basing on the above results, the behaviors of O₃ and PMS on FFeZn-M during FFeZn-M/PMS/O₃ process were inferred. When O₃, PMS and FFeZn-M co-occurred, the most likely site for PMS and O₃ adsorption was Zn and Fe, respectively (discussed in Section 3.4.4). PMS was attracted by FFeZn-M through the hydrogen bond force and formed the metal-PMS ligand. Then, PMS donated its electron to the adjacent Zn species and finally formed ¹O₂ via the metal to ligand electron transfer [41]. The electron donated by PMS could be rapidly consumed by O₃. Therefore, the electron migration rate was further accelerated, which resulted in the greatest ¹O₂ formation in FFeZn-M/O₃/PMS process. Overall, the greater •OH and ¹O₂ in FFeZn-M/O₃/PMS process benefited for IBP degradation.

The contributions of ROS to IBP degradation were studied. TBA and DMSO were used as probe molecular for free •OH and surface bonded •OH, respectively. Fig. 6(a-b) showed that upon 5 mg L⁻¹ TBA addition, IBP removal was suppressed from 100% to 88.9%, but the further increase of TBA concentration did not result in the substantial inhibitory effects. However, the introduction of 5–15 mg L⁻¹ DMSO suppressed IBP degradation to 75.2%, 70.6%, and 65.7%, respectively. The greater inhibition caused by DMSO demonstrated the greater contribution of surface bonded •OH [12]. Methanol was used to quench both free SO₄•⁻ and •OH. As depicted in Fig. 6(c), IBP degradation gradually declined with methanol concentration and the minimal IBP removal was 78.1% with the addition of 15 mg L⁻¹ methanol, which was similar to that in FFeZn-M/O₃/PMS process with 15 mg L⁻¹ TBA. This result indicated that SO₄•⁻ had little contribution to IBP degradation. The introduction of 5–15 mg L⁻¹ furfuryl alcohol suppressed IBP degradation from 100% to 84.6%, 80.7%, and 78.9%, respectively, suggesting the involvement of ¹O₂ in IBP degradation (Fig. 6(d)). Furthermore, p-BQ was selected to capture O₂•⁻. IBP decreased to 85.9% after introducing 5 mg L⁻¹ p-BQ. But the further increase of p-BQ even promoted the IBP degradation (Fig. 6(e)). On the one hand, the quinone groups in p-BQ could promote the activation of O₃ and PMS, thereby increasing the concentration of •OH and SO₄•⁻ [48,49]. On the other hand, besides quenching O₂•⁻, p-BQ could trigger the decomposition of PMS and produce ¹O₂ [8]. Basing on the above results, IBP oxidation in FFeZn-M/O₃/PMS process was associated with radical routes of •OH and non-radical route of ¹O₂.

3.4.2. Interfacial activation of PMS

The Lewis acid sites on metal silicon based materials were the main area for PMS and O₃ activation. They had a strong affinity toward the nucleophilic PMS and O₃ molecular [14,52]. The interfacial behaviors of
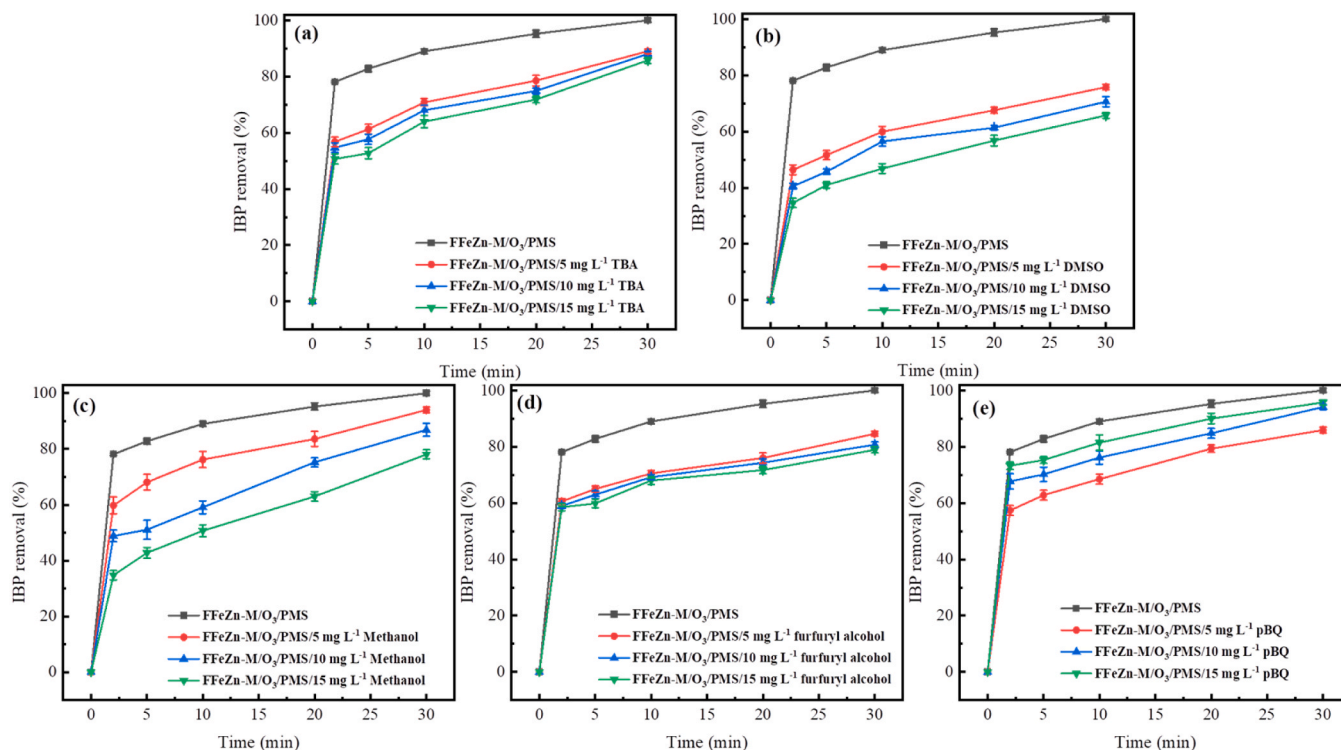
Fig. 6. Effect of TBA (a), DMSO(b), methanol(c), furfuryl alchohol (d) and pBQ (e) for IBP removal (Reaction condition: IBP concentration: 10 mg L^{-1}; initial pH: 5.0; total volume: 1.0 L; PS dosage: 0.4 g/L; O_3 output: 50 mg/h; flow rate: 1.0 L/min, catalyst concentration: 0.5 g/L).

O_3 and PMS with Fe and Zn sites on FFeZn-M were explored by in situ ATR-FTIR and in situ Raman.

As depicted in Fig. 7(a), there were characteristic surface hydroxyl peaks at 1633 and 3213–3585 cm^{-1} on the surface of FFeZn-M for FFeZn-M/O_3, FFeZn-M/PMS, and FFeZn-M/O_3/PMS processes [53]. The surface hydroxyl signals in FFeZn-M/O_3 and FFeZn-M/PMS processes were stronger over that of FFeZn-M/O_3/PMS process, which demonstrated that the more surface hydroxyl groups were involved in O_3 and PMS activation in FFeZn-M/O_3/PMS [54]. Additionally, FFeZn-M/PMS exhibited significant characteristic peaks at 900–1340 cm^{-1}, which was associated with the S-O stretch on PMS [53,55]. However, this characteristic peak was not observed in FFeZn-M/O_3/PMS process. The above results showed that FFeZn-M possessed a strong affinity for PMS but it had limited activity in PMS activation. Only when O_3 and PMS

coexisted on FFeZn-M, could the effective activation occur. In the in-situ Raman spectra of FFeZn-M/PMS (Fig. 7(b)), there existed two characteristic peaks of S-O bond at 856 and 1109 cm^{-1} and peroxy bonds (-O-O-) binding with metal sites at 836 cm^{-1}, which further confirmed that PMS could be absorbed on FFeZn-M and form $\equiv$Fe-O-O-SO_3^- and $\equiv$Zn-O-O-SO_3^- [55–57]. The peak at 978 cm^{-1} was SO_4^{2-} of PMS and its intensity decreased significantly in FFeZn-M/O_3/PMS process, which was mainly resulted from the decomposition of PMS caused by O_3 [26]. Moreover, the intensity of peroxy bonds was enhanced after introducing O_3, suggesting that the adsorption sites for O_3 was different from that of PMS.

3.4.3. Interfacial electron transfer

The activations of O_3 and PMS were all involved with the electron
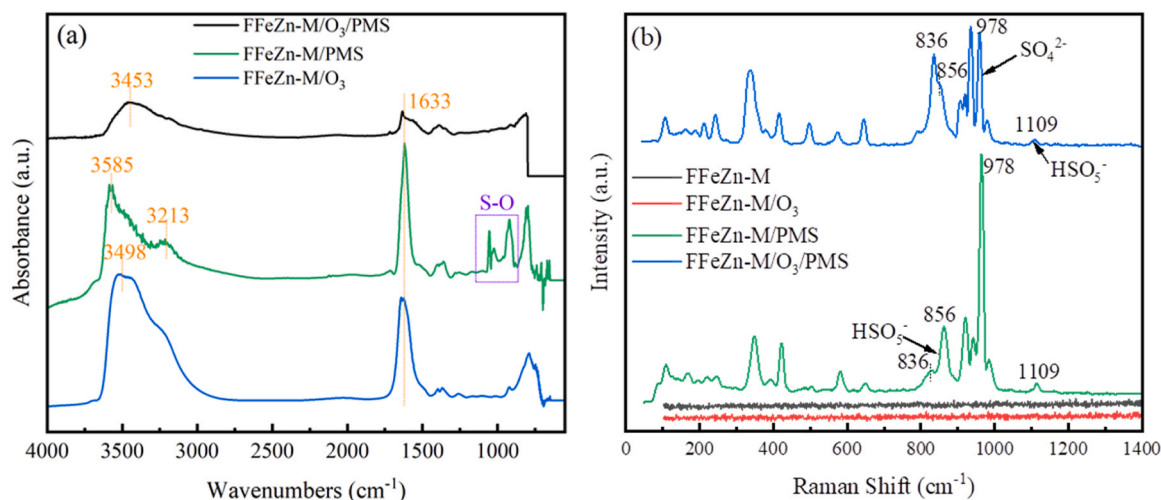
Fig. 7. FTIR (a) and Raman (b) spectra of different processes.

migration, which would alter the valence of metal species. To investigate interfacial electron behaviors of PMS and O_3 on FFeZn-M, XPS was carried out to explore the change of chemical states of Fe and Zn during reaction. As demonstrated in Fig. 8(a), the half-widths of Fe2p3/2 and Fe2p1/2 peaks in Fe 2p spectrum were broader for the used FFeZn-M. Additionally, the binding energies of Fe 2p3/2 and Fe 2p1/2 decreased from 711.5 and 725.0 eV to 711.2 and 724.3 eV, respectively, suggesting that oxidation status of Fe was altered during the reaction [58]. After the FFeZn-M/O_3/PMS process, the characteristic peaks of Fe^{3+} and Fe^{2+} could be obtained by fitting Fe2p3/2 and Fe2p1/2, respectively. Hardly any Fe^{2+} could be observed in raw FFeZn-M. But it existed in the used FFeZn-M with Fe2p3/2 and Fe2p1/2 occurring at 709.6 and 722.3 eV, respectively [59]. Moreover, the binding energies of Fe2p3/2 and Fe2p1/2 for Fe^{3+} decreased from 712.6 to 711.5 eV and 725.9 to 725.0 eV. The changes in Fe 2p spectrum suggested that there were continuous electron migration toward Fe site during FFeZn-M/O_3/PMS process [60]. As depicted in Fig. 8(b), Zn in fresh FFeZn-M displayed the distinctive peaks of Zn2p3/2 and Zn2p1/2 at 1022.5 and 1045.8 eV. They shifted to 1021.7 and 1045.5 eV after FFeZn-M/O_3/PMS process, which was corresponded to the formation of $\equiv$Zn-O-O-SO_3. Under the electron withdrawing effect of Si-F and its adjacent Fe, electron of surface bonded PMS would migrate toward Fe site, generating $SO_5\bullet$ and Fe^{2+}. Then, Fe could activate its surface bonded O_3 into $\bullet$OH. The self-interaction of $SO_5\bullet$ would yield $^1O_2$.

LSV was further used to study the electron transfer of FFeZn-M/O_3/PMS process (Fig. 9). The initial current of FFeZn-M electrode was -1.2 μA when applied voltage was -1.0 V. The introduction of O_3 could enhance the current to -1.4 μA, which demonstrated that FFeZn-M could activate O_3. However, the introduction of PMS slightly decreased the current intensity to -1.1 μA when compared with that of FFeZn-M electrode. The decrease in current intensity indicated the reverse electron flow between FFeZn-M-PMS and FFeZn-M-O_3 [61]. The
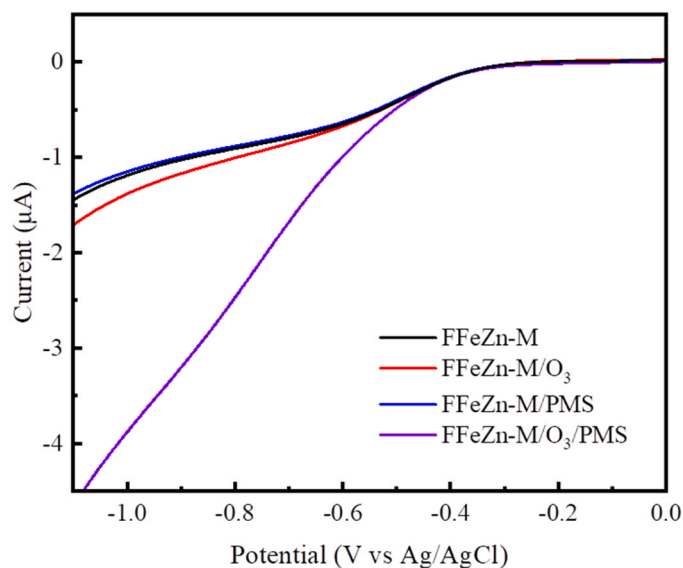
Fig. 9. Influence of O_3 and/or PMS on LSV of FFeZn-M.

addition of PMS to the FFeZn-M/O_3 system resulted in a significant increase in the initial current (-3.8 μA), signifying that the synergy of PMS and O_3 could indeed promote the interfacial electron transfer efficiency of FFeZn-M.

3.4.4. DFT simulations

For the sake of investigating the interfacial behavior of O_3 and PMS on FFeZn-M, DFT calculations were conducted. To model FeZn-M and FFeZn-M, a silica cluster was used. The Si atoms in the silica cluster were
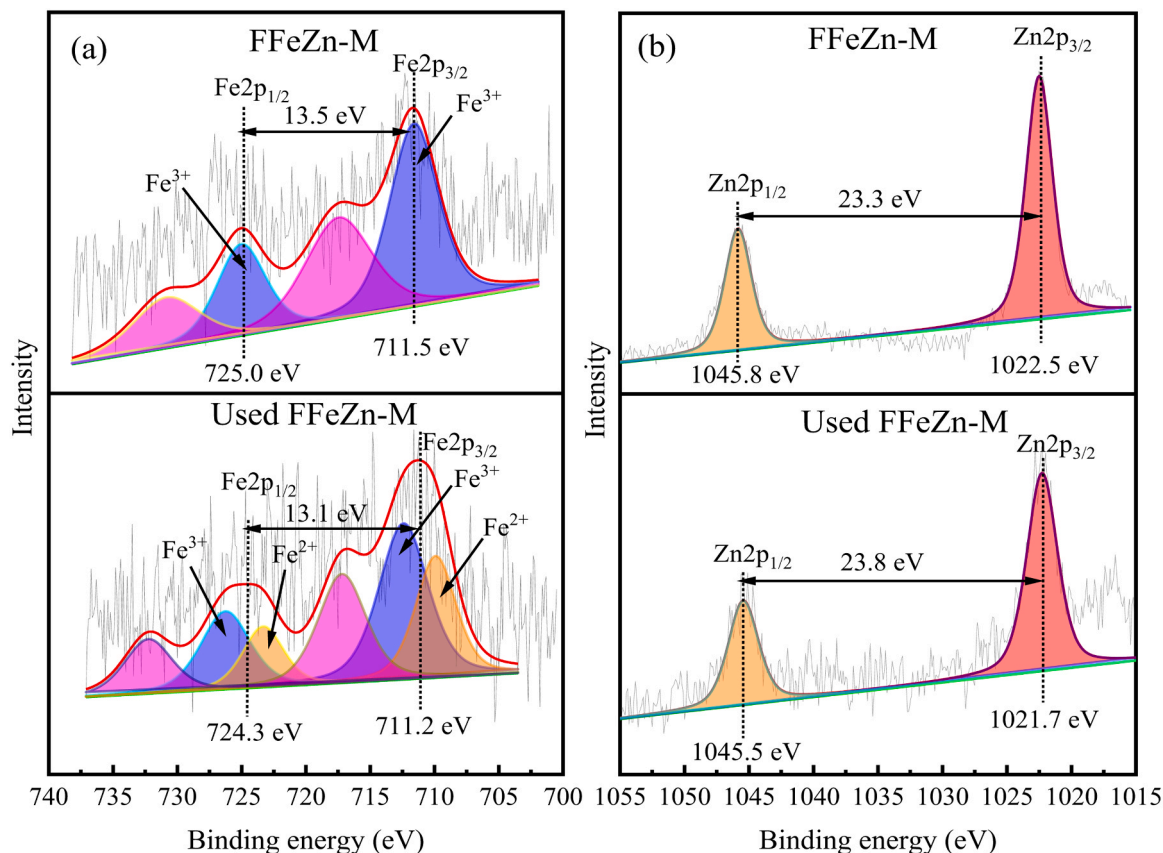
Fig. 8. XPS spectra of Fe(a) and Zn(b) of fresh and used FFeZn-M.

substituted with the specific metal atom (Fe or Zn) and Si-OH was substituted by F atom (Fig. S12). As shown in Table 1, the adsorption energies of O$_3$ and PMS on catalysts were calculated. The O$_3$ adsorption energies were calculated as − 1.97 and − 1.93 eV for Zn and Fe sites, respectively. And it increased to − 1.99 and − 1.95 eV for FFeZn-M. Therefore, it could be deduced that the doping of F atom could increase the affinity of FFeZn-M to O$_3$. As for the adsorption of PMS, the PMS adsorption energy on Fe site of FFeZn-M was − 1.89 eV. But it was − 2.86 eV when PMS was abs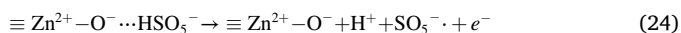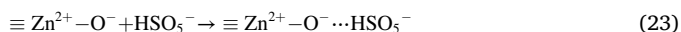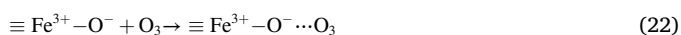orbed near Zn center. Obviously, PMS exhibited a higher tendency to be absorbed at the Zn site while O$_3$ was likely to be absorbed by Fe site.

The residual O$_3$ and PMS concentrations were also measured to explore their convey rate during heterogeneous process. As it could be observed in Fig. 10(a), the residual O$_3$ in sole O$_3$ was 1.22 mg L^{-1}. And it decreased to 0.75 or 0.44 mg L^{-1} after introducing PMS or FFeZn-M, demonstrating that FFeZn-M showed the greater O$_3$ activation ability than that of PMS. The couple of FFeZn-M, PMS and O$_3$ presented the lowest residual O$_3$ concentration of 0.22 mg L^{-1}, which suggested the greatest O$_3$ utility rate. Similarly, for the case of PMS concentration (Fig. 10(b)), PMS was stable and its convey rate was only 15.0% in 30 min. Residual PMS concentration in O$_3$/PMS process was 0.26 mg L^{-1}. The greater PMS existed in FFeZn-M/PMS process (about 0.28 mg L^{-1}), indicating the limited ability of FFeZn-M in activating PMS, which was consistent with former analysis. As for FFeZn-M/O$_3$/PMS system, only 0.17 mg L^{-1} PMS was remained, with the convey rate reaching 57.5%. The above results successfully confirmed the great ability of FFeZn-M in activating PMS and O$_3$.

Charge difference densities were also utilized to investigate the migration of interfacial electrons. As shown in Fig. 11, PMS was absorbed on FFeZn-M's surface through the outer-sphere interaction, which was accompanied with the electron loss on PMS (known as the ligand-to-metal electron transfer reaction) [41]. Compared with that of sole O$_3$ on FFeZn-M, the distance between O$_3$ with FFeZn-M was much closer when O$_3$ and PMS co-existed on FFeZn-M. Additionally, there were more obvious electron accumulation between terminal O of O$_3$ near Fe, which resulted in the formation of •O$_3^-$. The generated •O$_3^-$ would then undergo the radical chain reaction to form •OH.
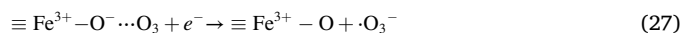
Basing on the above results, the synergetic function among FFeZn-M, O$_3$ and PMS was summarized as following: Fe and Zn on FFeZn-M were serving as Lewis acid for absorbing O$_3$ and PMS under the function of H bonding and electrostatic interactions (Eqs.22–23). Because Zn had the greater electron potential over Fe site, the electron from PMS was seized by Zn and then flowed to Fe site for the handy activation of O$_3$. The loss of electron on PMS would yield •SO$_5^-$, which was one of the important intermediates for generating ^{1}O$_2$ (Eqs.24–26) [8]. The electron from PMS would be utilized by O$_3$ to generate •O$_3^-$, which was eventually transformed in to •OH (Eqs.27–29) [62].

$$\equiv Fe^{3+}-O^- + O_3 \rightarrow \equiv Fe^{3+}-O^-\cdots O_3 \tag{22}$$

$$\equiv Zn^{2+}-O^- + HSO_5^- \rightarrow \equiv Zn^{2+}-O^-\cdots HSO_5^- \tag{23}$$

$$\equiv Zn^{2+}-O^-\cdots HSO_5^- \rightarrow \equiv Zn^{2+}-O^- + H^+ + SO_5^-\cdot + e^- \tag{24}$$

$$SO_5^-\cdot + SO_5^-\cdot \rightarrow S_2O_8^{2-} + {}^1O_2 \tag{25}$$

$$SO_5^-\cdot + SO_5^-\cdot \rightarrow 2SO_4^{2-} + {}^1O_2 \tag{26}$$

Table 1
Adsorption energy of O$_3$ and PMS on different sites with different orientations.

Adsorbents	E$_{ad}$ of FeZn-M (eV)		E$_{ad}$ of FFeZn-M (eV)	
	Fe	Zn	Fe	Zn
O$_3$	-1.93	-1.97	-1.95	-1.99
PMS	-1.81	-1.98	-1.89	-2.86

$$\equiv Fe^{3+}-O^-\cdots O_3 + e^- \rightarrow \equiv Fe^{3+}-O+\cdot O_3^- \tag{27}$$

$$O_3^-\cdot + H^+ \rightarrow HO_3\cdot \tag{28}$$

$$HO_3\cdot \rightarrow \cdot OH + O_2 \tag{29}$$

### 3.5. IBP degradation path and toxic assessment of intermediates

To better study the IBP degradation mechanism by FFeZn-M/O$_3$/PMS process, the intermediates were detected by GC-MS. 20 IBP degradation intermediates were detected and three IBP degradation pathways were deduced. IBP oxidation during FFeZn-M/O$_3$/PMS process was associated with hydroxylation, decarboxylation, demethylation, hydrogen abstraction, and ring-opening reactions.

Hydroxylation was identified as the initial step for IBP oxidation, with SO$_4$•$^-$, •OH, and ^{1}O$_2$ acting as electrophilic regents. In path I, hydroxylation occurred at the benzene ring, isobutyl group, and propanoic acid group of IBP, resulting in the formation of P1–1, P1–2, and P1–3 with m/z of 222.13. Additionally, when IBP was attacked by •OH, it was transformed into P2 (m/z = 239.13) [56,63]. The subsequent oxidation of the hydroxylated products led to the decarboxylation of P1–2, generating P3. Step-by-step demethylation of P1-P3 then produced P4, P5, and P6 with m/z values of 161.17, 162.10, and 134.11, respectively. Path II involved the detachment of the propanoic acid group from benzene ring, generating P7 (m/z = 150.17) and P12 (m/z = 90.05). Furthermore, P7 underwent further hydroxylation and demethylation to form P8 (m/z = 90.05). In Path III, decarboxylation first occurred on IBP, yielding P3. P3 then underwent hydroxylation and demethylation, leading to the formation of P9. Because of the lack of H atom in adjacent C atom, the oxidation of -OH on P9 generated P10 with two ketonic carbonyl groups. The further demethylation and decarboxylation of P10 resulted in the generation of P11 with m/z = 138.02. As the oxidation continued, the aromatic ring was opened, leading to the formation of various small molecule carboxylic acids like P12-P19. These organic acids were resistant to the direct oxidation by O$_3$ and PMS. However, they were easily attacked by SO$_4$•$^-$ and •OH, which enhanced TOC removal [64]..

The acute toxicity of intermediates toward daphnia, fish, and green algae were evaluated by ECOSAR (Table S3) [65]. Except for the intermediates of P3-P8, the toxic of hydroxylated IBP and the low molecular weight intermediates (P9-P19) were much lower than that of IBP. Though several toxic intermediates were produced, by prolonging the reaction time, the degradation of IBP into nontoxic products would be achieved.

4. Conclusions

This study explored the activation mechanism of O$_3$/PMS process by FFeZn-M with IBP acting as model pollutant. Comparative characterizations and DFT calculations demonstrated that the incorporation of F, Fe and Zn successfully constructed areas with large potential differences on the surface of FFeZn-M, which benefited for the electron migration from PMS to O$_3$. FFeZn-M/O$_3$/PMS process was highly effective in degrading IBP, achieving 100% IBP removal after only 30 min and 60.9% TOC removal after 60 min. It performed best under neutral pH conditions, and the presence of humic acid promoted IBP degradation. Lewis acid sites played a vital role in activating PMS and O$_3$. •OH and ^{1}O$_2$ were the primary active oxygen species for degrading IBP. PMS was bonded with FFeZn-M through the outer-sphere interaction and then donated its electron under the function of the ligand-to-metal electron transfer. The electron was transferred in the direction of Zn-O-Fe and finally used to activate surface O$_3$ under the driving of potential differences between Fe and Zn. These findings demonstrated that FFeZn-M was a promising candidate for heterogeneous O$_3$/PMS process.
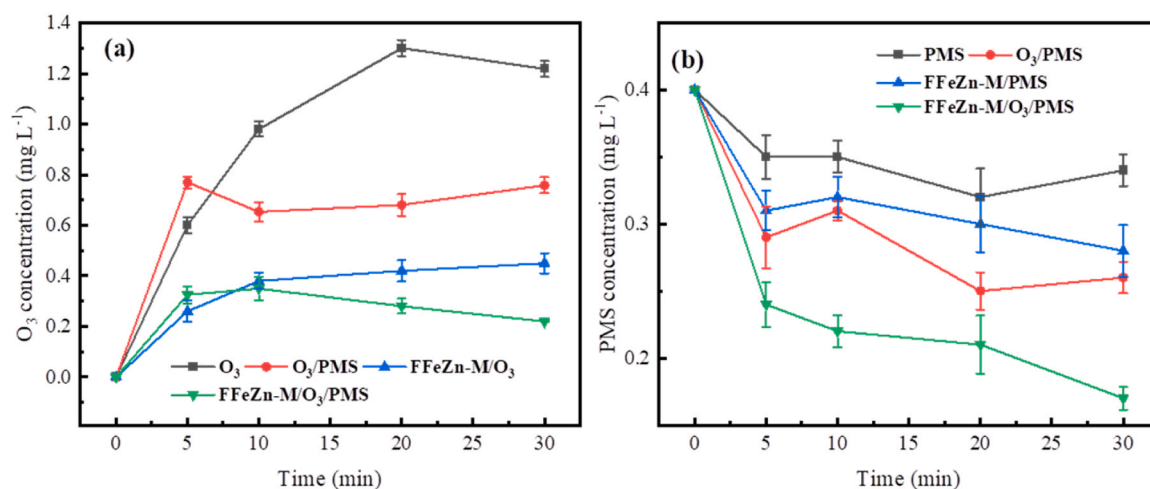
Fig. 10. Residual O_3 and PMS concentration during different processes.
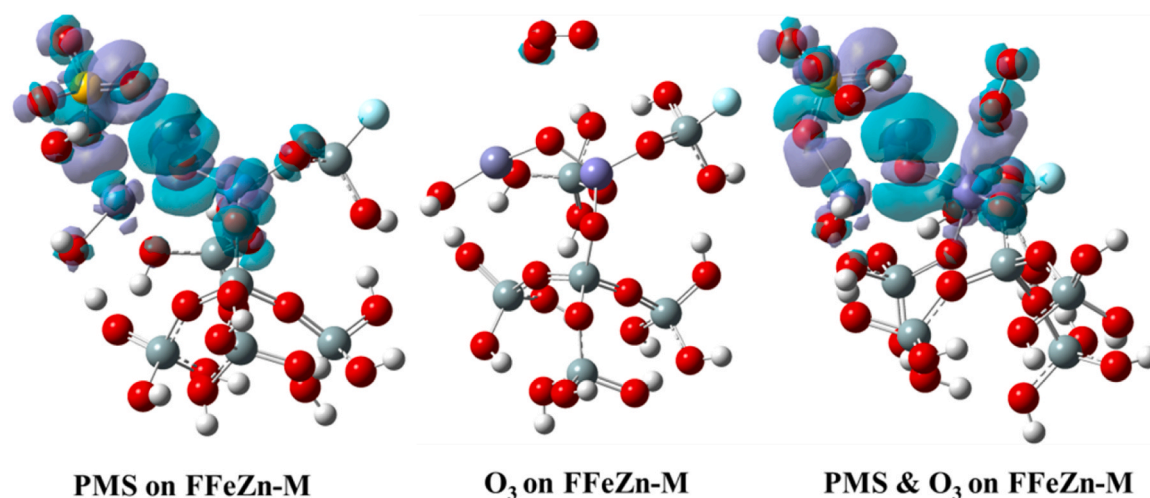
Fig. 11. Charge different density of O_3 and PMS absorbed on FFeZn-M (purple for electron accumulation and cyan for electron loss, isosurface value=0.002).
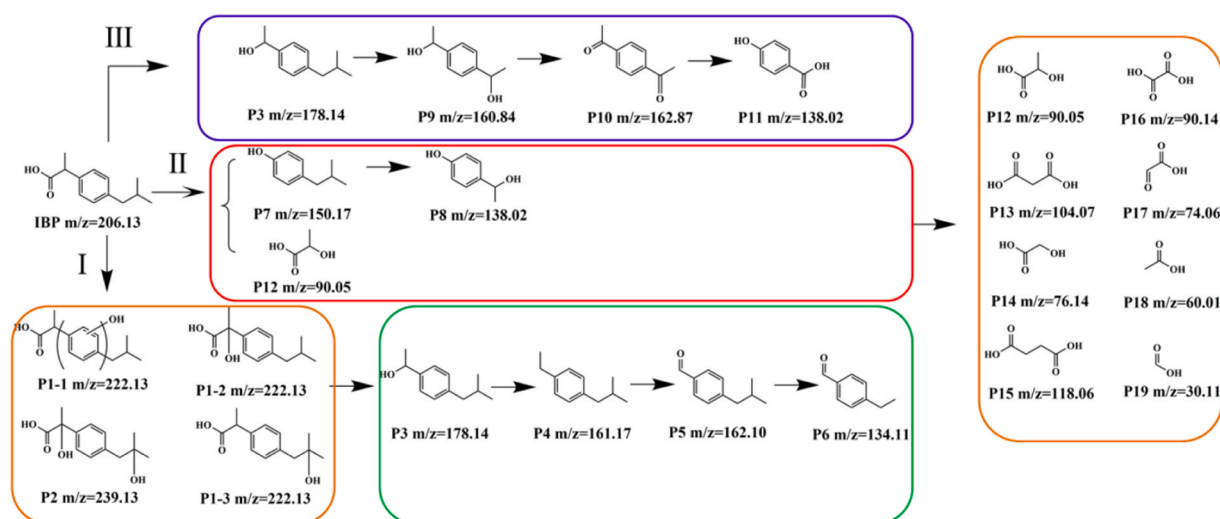
Fig. 12. Proposed degradation pathway of IBP during FFeZn-M/O_3/PMS.

CRediT authorship contribution statement

Li Xukai: Investigation, Methodology, Supervision. **Yi Yunqiang:** Investigation, Software. **Liu Dongpo:** Investigation, Methodology. **Tian Yingjing:** Data curation, Investigation, Methodology. **Chen Weirui:** Conceptualization, Data curation, Funding acquisition, Investigation, Writing – original draft. **Li Laisheng:** Conceptualization, Funding acquisition, Supervision, Writing – review & editing. **Tang Bing:** Investigation, Methodology. **Li Ping:** Investigation, Methodology. **Bin Liying:** Investigation, Methodology. **Wang Jing:** Funding acquisition, Supervision.

Declaration of Competing Interest

The authors declare that they have no known competing financial interests or personal relationships that could have appeared to influence the work reported in this paper.

Data Availability

No data was used for the research described in the article.

Acknowledgments

Appendix A. Supporting information

Supplementary data associated with this article can be found in the online version at doi:10.1016/j.apcatb.2023.123608.

References

[1] V. Singh, S. Suthar, Occurrence, seasonal variation, mass loading and fate of pharmaceuticals and personal care products (PPCPs) in sewage treatment plants in cities of upper Ganges bank, India, J. Water Process Eng. 44 (2021) 102399.

[2] L. Yang, T. Wang, Y. Zhou, B. Shi, R. Bi, J. Meng, Contamination, source and potential risks of pharmaceuticals and personal products (PPCPs) in Baiyangdian Basin, an intensive human intervention area, China, Sci. Total Environ. 760 (2021) 144080.

[3] S. Li, X. Fan, M. Gu, G. Cagnetta, J. Huang, G. Yu, Confined-space strategy for anchoring catalytic nanoparticles on Si-OH by ball milling for enhanced O₃/PMS oxidation of ciprofloxacin, Chem. Eng. J. 429 (2022) 132318.

[4] Z.T. How, Z. Fang, P. Chelme-Ayala, S.O. Ganiyu, X. Zhang, B. Xu, C. Chen, M. Gamal El-Din, Ozone-activated peroxymonosulfate (O₃/PMS) process for the removal of model naphthenic acids compounds: Kinetics, reactivity, and contribution of oxidative species, J. Environ. Chem. Eng. 11 (3) (2023) 109935.

[5] Y. Mao, H. Dong, S. Liu, L. Zhang, Z. Qiang, Accelerated oxidation of iopamidol by ozone/peroxymonosulfate (O₃/PMS) process: Kinetics, mechanism, and simultaneous reduction of iodinated disinfection by-product formation potential, Water Res. 173 (2020) 115615.

[6] G. Liao, P. Xu, P. Lu, X. Qing, Z. Yu, Y. Chang, W. Chen, Y. Tang, J. Wang, X. Wang, X. Li, L. Li, D. Xia, Dramatic enhancement of mineralization capability for ozone/ peroxymonosulfate process by single atom Co/CMK-3 catalyst, Sep. Purif. Technol. 287 (2022) 120582.

[7] Q. Sun, Y. Wang, L. Li, J. Bing, Y. Wang, H. Yan, Mechanism for enhanced degradation of clofibric acid in aqueous by catalytic ozonation over MnOₓ/SBA-15, J. Hazard. Mater. 286 (2015) 276–284.

[8] W. Chen, X. Li, X. Wei, G. Liao, J. Wang, L. Li, Activation of peroxymonosulfate for degrading ibuprofen via single atom Cu anchored by carbon skeleton and chlorine atom: The radical and non-radical pathways, Sci. Total Environ. 858 (Pt 3) (2023) 160097.

[9] N. Jaafarzadeh, F. Ghanbari, M. Ahmadi, Efficient degradation of 2,4-dichloro-phenoxyacetic acid by peroxymonosulfate/magnetic copper ferrite nanoparticles/ ozone: A novel combination of advanced oxidation processes, Chem. Eng. J. 320 (2017) 436–447.

[10] L.H. Nguyen, X.H. Nguyen, V.L. Nguyen, V.T. Pham, V.N. Thai, T.L. Luu, V.H. Tap, H. Nghiem Le, Enhanced degradation of cefalexin using Co₂SnO₄@rGO as an effective peroxymonosulfate activator in hybrid ozonation system, J. Environ. Chem. Eng. 11 (3) (2023) 110076.

[11] W. Chen, H. He, J. Liang, X. Wei, X. Li, J. Wang, L. Li, A comprehensive review on metal based active sites and their interaction with O₃ during heterogeneous catalytic ozonation process: types, regulation and authentication, J. Hazard. Mater. 443(Pt B) (2023) 130302.

[12] W. Chen, Y. Bao, X. Li, J. Huang, J. Xie, L. Li, Role of SiF groups in enhancing interfacial reaction of Fe-MCM-41 for pollutant removal with ozone, J. Hazard. Mater. 393 (2020) 122387.

[13] D. Liu, M. Lin, W. Chen, J. Wang, X. Guo, X. Li, L. Li, Enhancing catalytic ozonation activity of MCM-41 via one-step incorporating fluorine and iron: The interfacial reaction induced by hydrophobic sites and Lewis acid sites, Chemosphere 292 (2022) 133544.

[14] Q. Yang, X. Niu, Y. Zhu, Y. Cui, Y. Chao, P. Liang, C. Zhang, S. Wang, Modulating anion defect in La₀.₆Sr₀.₄Co₀.₈Fe₀.₂O₃-δ for enhanced catalytic performance on peroxymonosulfate activation: importance of hydrated electrons and metal-oxygen covalency, J. Hazard. Mater. 432 (2022) 128686.

[15] Q. Xia, D. Zhang, Z. Yao, Z. Jiang, Revealing the enhancing mechanisms of Fe-Cu bimetallic catalysts for the Fenton-like degradation of phenol, Chemosphere 289 (2022) 133195.

[16] F. Xie, W. Zhu, P. Lin, J. Zhang, Z. Hao, J. Zhang, T. Huang, A bimetallic (Co/Fe) modified nickel foam (NF) anode as the peroxymonosulfate (PMS) activator: characteristics and mechanism, Sep. Purif. Technol. 296 (2022) 121429.

[17] C. Cai, H. Zhang, X. Zhong, L. Hou, Ultrasound enhanced heterogeneous activation of peroxymonosulfate by a bimetallic Fe-Co/SBA-15 catalyst for the degradation of Orange II in water, J. Hazard. Mater. 283 (2015) 70–79.

[18] Y. Chen, K. Cui, T. Liu, M. Cui, Y. Ding, Y. Chen, W.W. Li, C.X. Li, Enhanced degradation of sulfamethoxazole by non-radical-dominated peroxymonosulfate activation with Co/Zn co-doped carbonaceous catalyst: synergy between Co and Zn, Sci. Total Environ. 850 (2022) 158055.

[19] H. Song, H. Cui, H. Song, F. Li, The effect of Zn–Fe modified S₂O₈²⁻/ZrO₂–Al₂O₃ catalyst for n-pentane hydroisomerization, Res. Chem. Intermed. 42 (4) (2015) 3029–3038.

[20] W. Chen, M. Lin, J. Zhou, X. Li, X. Wei, G. Liao, J. Wang, L. Li, The regulation of electron distribution within silicon acidic sites and its contribution to Ketoprofen ozonation, Sep. Purif. Technol. 309 (2023) 123113.

[21] X. Fang, Q. Wang, A. Zheng, Y. Liu, Y. Wang, X. Deng, H. Wu, F. Deng, M. He, P. Wu, Fluorine-planted titanosilicate with enhanced catalytic activity in alkene epoxidation with hydrogen peroxide, Catal. Sci. Technol. 2 (12) (2012) 2433.

[22] Y. Jia, S.K. Khanal, L. Yin, L. Sun, H. Lu, Influence of ibuprofen and its biotransformation products on different biological sludge systems and ecosystem, Environ. Int. 146 (2021) 106265.

[23] K.H. Hama Aziz, H. Miessner, S. Mueller, D. Kalass, D. Moeller, I. Khorshid, M.A. M. Rashid, Degradation of pharmaceutical diclofenac and ibuprofen in aqueous solution, a direct comparison of ozonation, photocatalysis, and non-thermal plasma, Chem. Eng. J. 313 (2017) 1033–1041.

[24] K.H.Hama Aziz, Heterogeneous catalytic activation of peroxydisulfate toward degradation of pharmaceuticals diclofenac and ibuprofen using scrap printed circuit board, RSC Adv. 13 (1) (2022) 115–128.

[25] X. Li, W. Chen, D. Liu, G. Liao, J. Wang, Y. Tang, L. Li, Enhancing water purification through F and Zn-modified Fe-MCM-41 catalytic ozonation, J. Hazard. Mater. 460 (2023) 132357.

[26] S. Li, J. Huang, X. Li, L. Li, The relation of interface electron transfer and PMS activation by the H-bonding interaction between composite metal and MCM-48 during sulfamethazine ozonation, Chem. Eng. J. 398 (2020) 125529.

[27] H. Bader, J. Hoigné, Determination of ozone in water by the indigo method, Water Res. 15 (4) (1981) 449–456.

[28] Gaussian 16, Revision B.01 M.J. Frisch, G.W. Trucks, H.B. Schlegel, G.E. Scuseria, M.A. Robb, J.R. Cheeseman, G. Scalmani, V. Barone, G.A. Petersson, H. Nakatsuji, X. Li, M. Caricato, A.V. Marenich, J. Bloino, B.G. Janesko, R. Gomperts, B. Mennucci, H.P. Hratchian, J.V. Ortiz, A. F.zmaylov, L. Sonnenberg, D. Williams-Young, F. Ding, F. Lipparini, F. Egidi, J. Goings, B. Peng, A. Petrone, T. Henderson, D. Ranasinghe, V.G. Zakrzewski, J. Gao, N. Rega, G. Zheng, W. Liang, M. Hada, M. Ehara, K. Toyota, R. Fukuda, J. Hasegawa, M. Ishida, T. Nakajima, Y. Honda, O. Kitao, H. Nakai, T. Vreven, K. Throssell, J.A. Montgomery Jr., J.E. Peralta, F. Ogliaro, M.J. Bearpark, J.J. Heyd, E.N. Brothers, K.N. Kudin, V.N. Staroverov, T. A. Keith, R. Kobayashi, J. Normand, K. Raghavachari, A.P. Rendell, J.C. Burant, S. S. Iyengar, J. Tomasi, M. Cossi, J.M. Millam, M. Klene, C. Adamo, R. ammi, J. W. Ochterski, R.L. Martin, K. Morokuma, O. Farkas, J.B. Foresman, D.J. Fox, Gaussian, Inc., Wallingford CT, 2016.

[29] F. Meng, S. Zhang, M. Zhang, Q. Zhong, The mechanism of Ce-MCM-41 catalyzed peroxone reaction into •OH and •O₂⁻ radicals for enhanced NO oxidation, Mol. Catal. 518 (2022) 112110.

[30] S. Shen, J. Chen, R.T. Koodali, Y. Hu, Q. Xiao, J. Zhou, X. Wang, L. Guo, Activation of MCM-41 mesoporous silica by transition-metal incorporation for photocatalytic hydrogen production, Appl. Catal. B: Environ. 150 151 (2014) 138–146.

[31] K. Winiarska, I. Szczygiel, R. Klimkiewicz, Manganese–zinc ferrite synthesis by the Sol–Gel autocombustion method. effect of the precursor on the ferrite's catalytic properties, Ind. Eng. Chem. Res. (2012), 121226133853001.

[32] W. Zhou, J. Liu, L. Lin, X. Zhang, N. He, C. Liu, H. Guo, Enhanced dehydrogenative aromatization of propane by incorporating Fe and Pt into the Zn/HZSM-5 catalyst, Ind. Eng. Chem. Res. 57 (48) (2018) 16246–16256.

[33] G. Song, R. Gao, Z. Zhao, Y. Zhang, H. Tan, H. Li, D. Wang, Z. Sun, M. Feng, High-spin state Fe(III) doped TiO₂ for electrocatalytic nitrogen fixation induced by surface F modification, Appl. Catal. B: Environ. 301 (2022) 120809.

[34] Y. Yang, J. Jiang, X. Lu, J. Ma, Y. Liu, Production of sulfate radical and hydroxyl radical by reaction of ozone with peroxymonosulfate: a novel advanced oxidation process, Environ. Sci. Technol. 49 (12) (2015) 7330–7339.

[35] W.-D. Oh, Z. Dong, T.-T. Lim, Generation of sulfate radical through heterogeneous catalysis for organic contaminants removal: current development, challenges and prospects, Appl. Catal. B: Environ. 194 (2016) 169–201.

[36] S.S. Abu Amr, H.A. Aziz, M.N. Adlan, M.J.K. Bashir, Pretreatment of stabilized leachate using ozone/persulfate oxidation process, Chem. Eng. J. 221 (2013) 492–499.

[37] J. Wang, Y. Xie, G. Yu, L. Yin, J. Xiao, Y. Wang, W. Lv, Z. Sun, J.H. Kim, H. Cao, Manipulating selectivity of hydroxyl radical generation by single-atom catalysts in catalytic ozonation: surface or solution, Environ. Sci. Technol. 56 (24) (2022) 17753–17762.

[38] G. Yu, Y. Wang, H. Cao, H. Zhao, Y. Xie, Reactive oxygen species and catalytic active sites in heterogeneous catalytic ozonation for water purification, Environ. Sci. Technol. 54 (10) (2020) 5931–5946.

[39] Q. Sun, L. Li, H. Yan, X. Hong, K.S. Hui, Z. Pan, Influence of the surface hydroxyl groups of MnO_x/SBA-15 on heterogeneous catalytic ozonation of oxalic acid, Chem. Eng. J. 242 (2014) 348–356.

[40] L. Long, L. Su, W. Hu, S. Deng, C. Chen, F. Shen, M. Xu, G. Huang, G. Yang, Micro-mechanism of multi-pathway activation peroxymonosulfate by copper-doped cobalt silicate: the dual role of copper, Appl. Catal. B: Environ. 309 (2022) 121276.

[41] Y. Ding, L. Fu, X. Peng, M. Lei, C. Wang, J. Jiang, Copper catalysts for radical and nonradical persulfate based advanced oxidation processes: certainties and uncertainties, Chem. Eng. J. 427 (2022) 131776.

[42] M. Golshan, B. Kakavandi, M. Ahmadi, M. Azizi, Photocatalytic activation of peroxymonosulfate by TiO_2 anchored on cupper ferrite (TiO_2@$CuFe_2O_4$) into 2,4-D degradation: process feasibility, mechanism and pathway, J. Hazard. Mater. 359 (2018) 325–337.

[43] M.-P. Zhu, J.-C.E. Yang, D. Delai Sun, B. Yuan, M.-L. Fu, Deciphering the simultaneous removal of carbamazepine and metronidazole by monolithic Co_2AlO_4@Al_2O_3 activated peroxymonosulfate, Chem. Eng. J. 436 (2022) 135201.

[44] Q. Ye, J. Wu, P. Wu, J. Wang, W. Niu, S. Yang, M. Chen, S. Rehman, N. Zhu, Enhancing peroxymonosulfate activation of Fe-Al layered double hydroxide by dissolved organic matter: performance and mechanism, Water Res. 185 (2020) 116246.

[45] J. Zhang, C. Wang, M. Xiang, Y. Huang, L. Jin, Z. Yang, H. Li, Fe@Fe_2O_3 core-shell nanowires compounding humic acid enhanced catalysis removal 2,4,6-trichloro-phenol: performance and mechanism, Chem. Eng. J. 428 (2022) 131779.

[46] X. Duan, Z. Ao, L. Zhou, H. Sun, G. Wang, S. Wang, Occurrence of radical and nonradical pathways from carbocatalysts for aqueous and nonaqueous catalytic oxidation, Appl. Catal. B: Environ. 188 (2016) 98–105.

[47] P. Xiong, H. Zhang, G. Li, C. Liao, G. Jiang, Adsorption removal of ibuprofen and naproxen from aqueous solution with Cu-doped Mil-101(Fe), Sci. Total Environ. 797 (2021) 149179.

[48] M. Ahmad, A.L. Teel, R.J. Watts, Mechanism of persulfate activation by phenols, Environ. Sci. Technol. 47 (11) (2013) 5864–5871.

[49] G. Fang, J. Gao, D.D. Dionysiou, C. Liu, D. Zhou, Activation of persulfate by quinones: free radical reactions and implication for the degradation of PCBs, Environ. Sci. Technol. 47 (9) (2013) 4605–4611.

[50] Y. Liu, D. Wu, S. Peng, Y. Feng, Z. Liu, Enhanced mineralization of dimethyl phthalate by heterogeneous ozonation over nanostructured Cu-Fe-O surfaces: Synergistic effect and radical chain reactions, Sep. Purif. Technol. 209 (2019) 588–597.

[51] Y. Zhu, Z. Chen, Y. Gao, C. Hu, General synthesis of carbon and oxygen dual-doped graphitic carbon nitride via copolymerization for non-photochemical oxidation of organic pollutant, J. Hazard. Mater. 394 (2020) 122578.

[52] P. Zhang, Y. Yang, X. Duan, Y. Liu, S. Wang, Density functional theory calculations for insight into the heterocatalyst reactivity and mechanism in persulfate-based advanced oxidation reactions, ACS Catal. 11 (17) (2021) 11129–11159.

[53] A. Jawad, J. Lang, Z. Liao, A. Khan, J. Ifthikar, Z. Lv, S. Long, Z. Chen, Z. Chen, Activation of persulfate by CuOx@Co-LDH: a novel heterogeneous system for contaminant degradation with broad pH window and controlled leaching, Chem. Eng. J. 335 (2018) 548–559.

[54] J. Fan, Z. Zhao, Z. Ding, J. Liu, Synthesis of different crystallographic FeOOH catalysts for peroxymonosulfate activation towards organic matter degradation, RSC Adv. 8 (13) (2018) 7269–7279.

[55] T. Zhang, H. Zhu, J.P. Croue, Production of sulfate radical from peroxymonosulfate induced by a magnetically separable $CuFe_2O_4$ spinel in water: efficiency, stability, and mechanism, Environ. Sci. Technol. 47 (6) (2013) 2784–2791.

[56] Z. Ren, H. Romar, T. Varila, X. Xu, Z. Wang, M. Sillanpaa, T. Leiviska, Ibuprofen degradation using a Co-doped carbon matrix derived from peat as a peroxymonosulphate activator, Environ. Res. 193 (2021) 110564.

[57] W. Tan, W. Ren, C. Wang, Y. Fan, B. Deng, H. Lin, H. Zhang, Peroxymonosulfate activated with waste battery-based Mn-Fe oxides for pollutant removal: electron transfer mechanism, selective oxidation and LFER analysis, Chem. Eng. J. 394 (2020) 124864.

[58] Y. Ding, L. Zhu, N. Wang, H. Tang, Sulfate radicals induced degradation of tetrabromobisphenol A with nanoscaled magnetic $CuFe_2O_4$ as a heterogeneous catalyst of peroxymonosulfate, Appl. Catal. B: Environ. 129 (2013) 153–162.

[59] J. Wang, J. Tang, Fe-based Fenton-like catalysts for water treatment: Preparation, characterization and modification, Chemosphere 276 (2021) 130177.

[60] Y. Xu, J. Ai, H. Zhang, The mechanism of degradation of bisphenol A using the magnetically separable $CuFe_2O_4$/peroxymonosulfate heterogeneous oxidation process, J. Hazard. Mater. 309 (2016) 87–96.

[61] X. Mi, P. Wang, S. Xu, L. Su, H. Zhong, H. Wang, Y. Li, S. Zhan, Almost 100 % peroxymonosulfate conversion to singlet oxygen on single-atom CoN_{2+2} sites, Angew. Chem. 60 (9) (2021) 4588–4593.

[62] J. Nawrocki, B. Kasprzyk-Hordern, The efficiency and mechanisms of catalytic ozonation, Appl. Catal. B: Environ. 99(1-2) (2010) 27–42.

[63] X. Li, Y. Wang, S. Yuan, Z. Li, B. Wang, J. Huang, S. Deng, G. Yu, Degradation of the anti-inflammatory drug ibuprofen by electro-peroxone process, Water Res. 63 (2014) 81–93.

[64] W. Chen, X. Li, M. Liu, L. Li, Effective catalytic ozonation for oxalic acid degradation with bimetallic Fe-Cu-MCM-41: operation parameters and mechanism, J. Chem. Technol. Biotechnol. 92 (2017) 2862–2869.

[65] A. Massarsky, M.T. Donnell, E. de Gandiaga, J.S. Kozal, L. Garnick, J.A. Kubitz, S. M. Bartell, A.D. Monnot, Critical evaluation of ECOSAR and E-FAST platforms to predict ecological risks of PFAS, Environ. Adv. 8 (2022) 100221.